

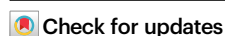


Bioelectrocatalytic carbon dioxide reduction by an engineered formate dehydrogenase from *Thermoanaerobacter kivui*

Received: 17 April 2024

Accepted: 29 October 2024

Published online: 17 November 2024

Weisong Liu^{1,2,3}, Kuncheng Zhang^{1,2,3}, Jiang Liu³, Yuanming Wang³, Meng Zhang^{3,4}, Huijuan Cui^{1,2,3}, Junsong Sun^{2,5} & Lingling Zhang^{1,2,3} ✉

Electrocatalytic carbon dioxide (CO₂) reduction by CO₂ reductases is a promising approach for biomanufacturing. Among all known biological or chemical catalysts, hydrogen-dependent carbon dioxide reductase from *Thermoanaerobacter kivui* (TkHDCR) possesses the highest activity toward CO₂ reduction. Herein, we engineer TkHDCR to generate an electro-responsive carbon dioxide reductase considering the safety and convenience. To achieve this purpose, a recombinant *Escherichia coli* TkHDCR overexpression system is established. The formate dehydrogenase is obtained via subunit truncation and rational design, which enables direct electron transfer (DET)-type bioelectrocatalysis with a near-zero overpotential. By applying a constant voltage of -500 mV (*vs.* SHE) to a mediated electrolytic cell, 22.8 ± 1.6 mM formate is synthesized in 16 h with an average production rate of 7.1 ± 0.5 $\mu\text{mol h}^{-1}\text{cm}^{-2}$, a Faradaic efficiency of 98.9% and a half-cell energy efficiency of 94.4%. This study provides an enzyme candidate for high efficient CO₂ reduction and opens up a way to develop paradigm for CO₂-based bio-manufacturing.

Carbon dioxide (CO₂) emissions pose significant environmental pressure, such as climate change. The effective reduction of CO₂ to fuels and chemicals is a promising approach for realizing a carbon-neutral economy¹. Liquid products such as formic acid and methanol are easy to store and transport, and their electrochemical production has been considered an attractive technology, especially in green chemical/biological transformation². The core issue in electrochemical CO₂ reduction lies in the design of electrocatalysts, including chemical electrocatalysts and bioelectrocatalysts. Chemical electrocatalysts are generally based on transition metals (e.g., Cu, Bi, Pb), and significant progress has been made in recent years. For instance, Xia et al. produced nearly 100% pure formic acid at a Pb electrode, which was derived from waste lead-acid batteries³. In addition, Sargent et al. reported that multi-carbon products were produced from CO₂

catalyzed by Cu-based catalysts in acidic media^{4,5}. Similarly, Yang et al. elucidated the breakthrough potential of Cu-based nanograins as electrocatalysts for generating C₂+ products⁶. However, chemical electrocatalysts encounter the challenges of high overpotentials and low atom economy due to the high energy barrier and inevitable side reactions. To address these issues, bioelectrocatalysts provide potential solutions. They can lower the activation energy more significantly than chemical catalysts can, thereby reducing the overpotential. Surely, enzymes are highly specific, ensuring efficiency, yield, and purity in the production of target products⁷.

Formate dehydrogenases (FDHs), which catalyze the interconversion between CO₂ and formate, have been intensively studied. Nielsen et al.⁸ and Moon et al.⁹ comprehensively reviewed FDHs with regard to organism sources, classification, structures, and electron donors.

¹Key Laboratory of Engineering Biology for Low-carbon Manufacturing, Tianjin Institute of Industrial Biotechnology, Chinese Academy of Sciences, 32 west 7th Avenue, Tianjin Airport Economic Area, Tianjin, China. ²University of Chinese Academy of Sciences, Beijing, China. ³In vitro Synthetic Biology Center, Tianjin Institute of Industrial Biotechnology, Chinese Academy of Sciences, Tianjin, China. ⁴College of Biotechnology, Tianjin University of Science and Technology, 9, 13th Avenue, Tianjin Economic and Technological Development Area, Tianjin, China. ⁵Shanghai Advanced Research Institute, Chinese Academy of Sciences, Shanghai, China. ✉e-mail: zhangll@tib.cas.cn

Notably, a majority of FDHs exhibit quite sluggish kinetics toward CO₂ reduction, with k_{cat} values of 0.01–1 s⁻¹. A few FDHs (e.g., FDHs from *Syntrophobacter fumaroxidans* and *Desulfovibrio vulgaris*) exhibit appreciable catalytic activity toward CO₂ reduction, they are prone to oxidize formate at relatively high catalytic rates⁹. Mo-dependent formylmethanofuran dehydrogenase exhibits preferential directionality for the reductive reaction¹⁰. However, the CO₂ reduction activity of formylmethanofuran dehydrogenase is 0.24 U mg⁻¹, which is insufficient for practical applications. Hydrogen-dependent carbon dioxide reductases (HDCRs) from *Acetobacter woodii* and *Thermoanaerobacter kivui* exhibit remarkable activity for CO₂ reduction, with k_{cat} values of 28 and 2654 s⁻¹, respectively, making them promising candidates for CO₂ biotransformation^{11,12}. Generally, the HDCR unit is a heterohexamer consisting of a formate dehydrogenase subunit, three electron transfer subunits, and two iron-iron hydrogenase subunits. Due to the multi-subunit structure and the complicated cofactors, the expression of HDCR is challenging. It was reported that the expression level of *TkHDCR* was as low as 0.05 mg L⁻¹ in its original strain. Therefore, it is desirable to establish efficient overexpression methods for sufficient *TkHDCR* production in common expression hosts, such as *Escherichia coli*.

Compared to hydrogen as an electron donor, electricity might be a better alternative because of its safety and convenience. Significant progress has been made in electricity-driven FDH catalysis. Reda et al. reported the first example of bioelectrocatalytic formate/CO₂ interconversion based on W-containing *SfFDH1* from *S. fumaroxidans*¹³. Reischer et al. studied the reversible bioelectrocatalysis of Mo-containing *EcFDH-H* from *E. coli* and utilized electrochemical and catalytic inhibition methodologies to comprehensively investigate the interconversion mechanism^{14,15}. Li et al. revealed the redox chemistry of the distal Fe-S cluster in *CIFDH* from *Clostridium ljungdahlii*, demonstrating its significant involvement in mediating electron transfer between the electrode and metal active site of the enzyme¹⁶. Strategies such as the employment of conductive polymers/electronic mediators and oriented immobilization were employed to improve the electron transfer efficiency. For example,

conductive polyaniline (PANI) hydrogel has been explored to fix *CIFDH* at the electrode, and a formate yield rate of 1.42 μmol h⁻¹ cm⁻² was reached¹⁷. An electron mediator such as benzylpropylviologen was also used to improve the rate of electron transfer from the electrode to *EcFDH*¹⁸. Directed immobilization of enzymes has emerged as a direct approach to improve the efficiency of direct electron transfer. Alvarez-Malmagro et al. designed a covalently immobilized strategy for *DvFDH* from *D. vulgaris* oriented immobilization on the electrode to improve the direct electron transfer rate¹⁹. Badiani et al. demonstrated that *DvFDH* was oriented fixed through electrostatic interaction between the negative spot of the Fe-S cluster and the positively functionalized electrode with -NHMe²⁺ group²⁰. In addition, Reischer et al. reported that the local environment of bioelectrocatalysis, including CO₂ concentration and pH, was also a key factor affecting the performance of CO₂ reduction^{21,22}. They also revealed that the fast CO₂ hydration kinetics could improve enzymatic CO₂ reduction catalysis^{23,24}.

In this work, we study the heterologous expression of *TkHDCR* in *E. coli* and its rational design. The maturation of W-MGD and Fe-Fe active sites involves several chaperone proteins. Through gene identification and codon optimization, plasmids and expression hosts are optimized. To replace the hydrogen supply with electricity, HDCR is truncated to different extents, generating the *FdhF_HycB3_HycB4*, *FdhF_HycB3*, and *FdhF* variants. Further structural adaptation of *FdhF_HycB3* is performed to generate the robust variant *FdhF_HycB3Δ159-184*. In formate bioelectrosynthesis, detailed bioelectrocatalytic kinetics and direct/mediated bioelectrosynthesis of *FdhF_HycB3Δ159-184* are studied to understand the catalytic mechanism of FDH catalysis/interfacial electron transfer and guide electro-assisted CO₂ biotransformation (Fig. 1).

Results and discussion

Heterologous expression of *TkHDCR* in *E. coli*

The challenges associated with the heterologous expression of *TkHDCR* include the unclear maturation mechanism of active sites and

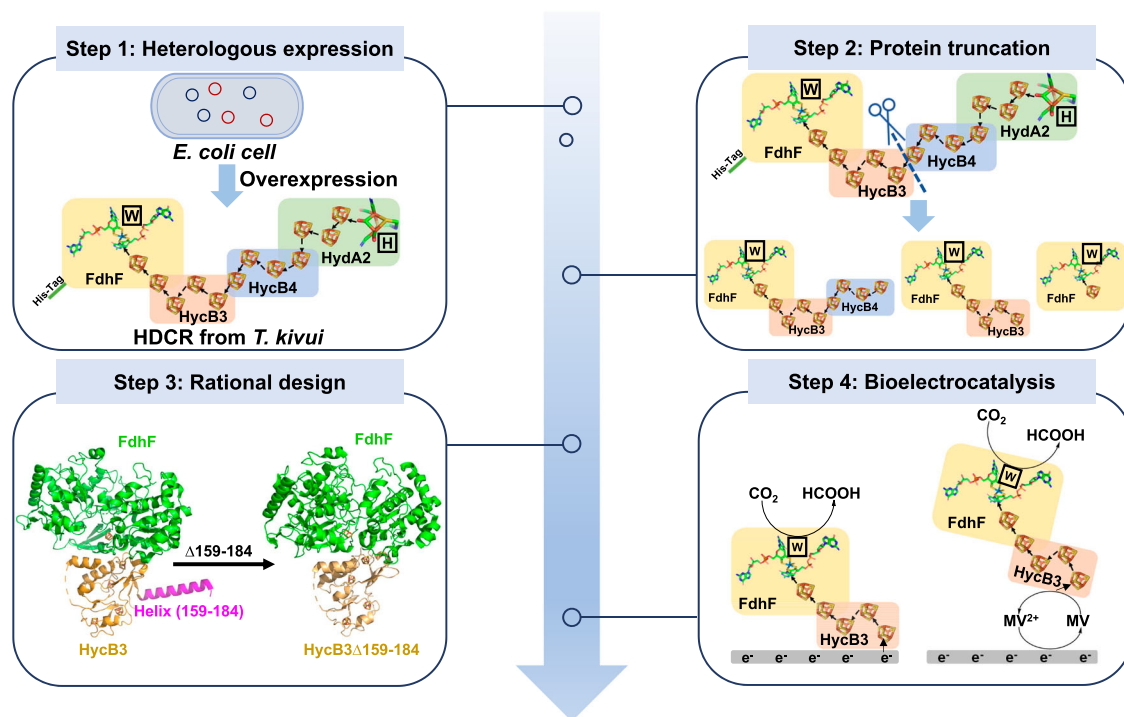


Fig. 1 | Schematic illustration of this study. Step 1: *TkHDCR* from *T. kivui* was heterologously expressed in *E. coli*, step 2: Formate dehydrogenase modules were acquired by truncation of *HDCR*, step 3: The robust variant *FdhF_HycB3Δ159-184* was obtained by rational design, step 4: Bioelectrocatalysis systems were constructed based on *FdhF_HycB3Δ159-184*.

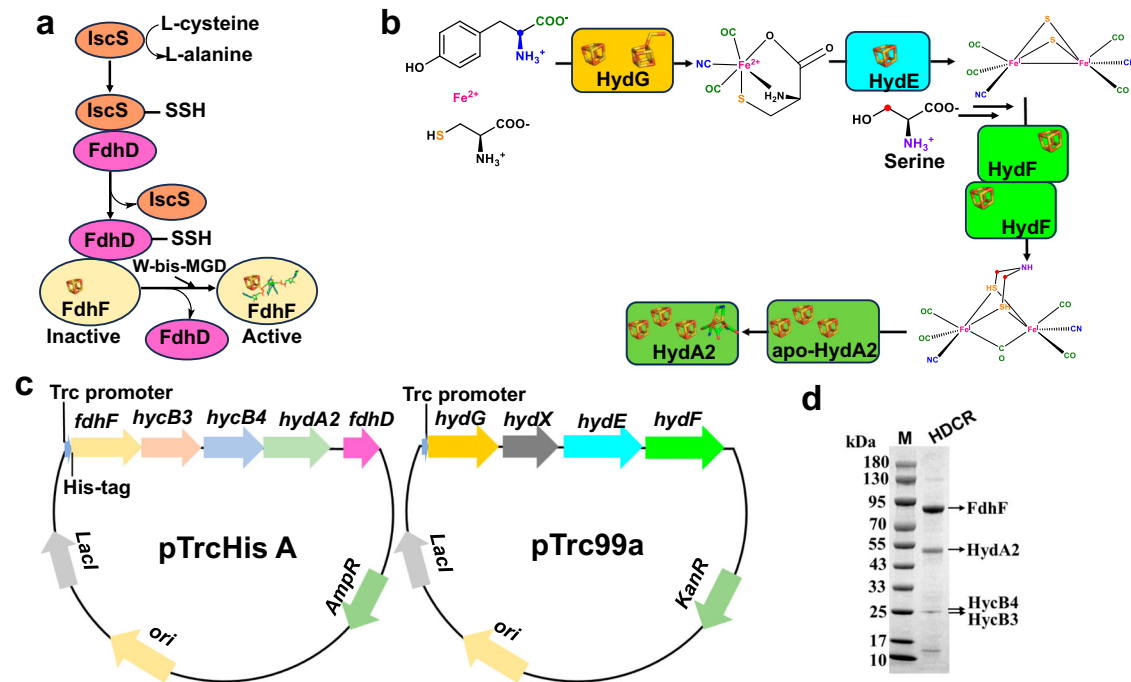


Fig. 2 | Strategy for heterologous expression of HDCR complex in *E. coli* MC1061. a The maturation process of FdhF was assisted by FdhD, IscS: L-cysteine desulfurases³⁰, **(b)** Biosynthesis of the catalytic H-cluster of [FeFe]-hydrogenase by HydG, HydE and HydF³³, **(c)** HDCR gene *fdhF*, *hycB3*, *hycB4*, *hydA2* and maturation factor gene *fdhD* from *T. kivui* were cloned and inserted into plasmid pTrcHis A, the

[FeFe]-hydrogenases mature proteins gene *hydG*, *hydX*, *hydE*, *hydF* from *Shewanella oneidensis* MR-1 were cloned and inserted into plasmid pTrc99a. **d** SDS-PAGE analysis of purified HDCR complex expressed in *E. coli* MC1061; M: standard protein marker. Three independent measurements were repeated. Source data are provided as a Source Data file.

the deficiency of auxiliary factors caused by the homologous disparity between *T. kivui* and *E. coli*. The maturation of W-bis-MGD and di-Fe active centers is crucial for the activation of *TkHDCR*. According to the cryo-EM structure, W-bis-MGDs are buried deep inside the FdhF subunit²⁵, suggesting that their insertion is intimately connected to protein folding and that the necessary chaperone is involved^{26,27}. Two possible genes, *fdhD*, and *fdhC*, were found in the *TkHDCR* gene cluster, while their corresponding proteins did not appear in the final mature HDCR. It is reasonable to speculate that these proteins might be molecular chaperones involved in HDCR maturation²⁸. However, the sequence identity between FdhD of *E. coli* and FdhD from *T. kivui* is only 27.3%, implying that FdhD from *E. coli* may not effectively assist the correct insertion of W-bis-MGD into the FdhF subunit of *T. kivui*, which is different from what is observed in *AwHDCR* expressed in *E. coli*²⁹. Therefore, the roles of the *fdhD* and *fdhC* genes from *T. kivui* were investigated experimentally (Supplementary Fig. 1). To investigate the role of FdhD and FdhC in the maturation of FdhF, the *fdhD* and *fdhC* genes were codon-optimized and cloned into plasmid pETDuet-1. As shown in Supplementary Fig. 1, the bands at 82.5 kDa were assigned to FdhF, but no activity is detected with respect to *fdhF*_{fdhC}, while *fdhF*_{fdhD} and *fdhF*_{fdhD}_{fdhC} show nearly equal activity towards formate oxidation (Data was not shown). This suggests that FdhD is necessary for the maturation of FdhF, but FdhC has less influence. As a consequence, FdhD is necessary for the functional integrity of FdhF, and it may catalyze the transfer of sulfur from L-cysteine desulfurase (IscS) to Mo/W-bis-MGD, forming the terminal sulfur ligand Mo/W=S and assisting in the assembly of mature Mo/W-bis-MGD into the active center of FDH (Fig. 2a)^{30,31}. The H-clusters of [FeFe]-hydrogenases also require accessory proteins for the maturation of the active center³². The chaperones HydE, HydF, and HydG are conserved, and their roles have been well studied (Fig. 2b)^{32–34}. [FeFe]-hydrogenases from *C. reinhardtii* and *C. pasteurianum* exhibited high-yield expression in *E. coli* along with the maturation proteins (HydG, HydX, HydE, and HydF) from *Shewanella oneidensis* MR-1³⁵. The HydG, HydE, and HydF

proteins from *T. kivui* exhibit sequence identities of 47.0%, 36.8%, and 49.1%, respectively, to their counterparts in *Shewanella oneidensis* MR-1. On this basis, the pACYCDuet-*hydGXEF* plasmid was constructed by cloning the maturase gene cluster, *hydG*, *hydX*, *hydE*, and *hydF* from *Shewanella oneidensis* MR-1 (Supplementary Fig. 2a).

When pETDuet-*hdcR* and pACYCDuet-*hydGXEF* were both transformed into *E. coli* BL21 (DE3) for *TkHDCR* overexpression (Supplementary Fig. 2a), only the FdhF subunit was observed (Supplementary Fig. 2b, lane 1). When an extra His-tag was fused at the C-terminus of *HydA2*, *HydA2* can be captured (Supplementary Fig. 2b, lane 2), suggesting unsuccessful expression of the *HycB3* and *HycB4* subunits or improper assembly of each subunit of the HDCR complex. The expression of sole *HycB3* and sole *HycB4* formed massive inclusion bodies, which was confirmed to be the reason for the failure of *TkHDCR* complex assembly (Supplementary Fig. 2c). In these circumstances, the vector pTrcHis was used because the Trc promoter is weaker than the T7 promoter, allowing for mild cofactor maturation. It has been widely employed in the expression of multi-subunit enzymes or insoluble enzyme^{36,37}. The plasmid pTrcHisA-*hdcR*, along with its counterpart pTrc99a-*hydGXEF*, was constructed and expressed in *E. coli* MC1061 (Fig. 2c and Supplementary Fig. 3). Remarkably, all four subunits of *TkHDCR*, FdhF, *HydA2*, *HycB4*, and *HycB3*, were distinctly observed (Fig. 2d), demonstrating successful expression of the *TkHDCR* complex. Using methyl viologen (MV²⁺) and reduced methyl viologen (MV) to assess catalytic activity, respectively, the obtained HDCR exhibited a CO₂ reduction activity (MV: CO₂-oxidoreductase activity) of 1318.7 min⁻¹ at 30 °C and a formate oxidation activity (formate: MV²⁺-oxidoreductase activity) of 202.9 min⁻¹. This achievement represents the successful production of active HDCR from *T. kivui* in *E. coli*, revealing a convenient and expeditious method.

Engineering of *TkHDCR* to acquire FDH module

To obtain the FDH module, *HydA2* and its possible electron-transfer counterparts were gradually truncated from the *TkHDCR*³⁸, generating

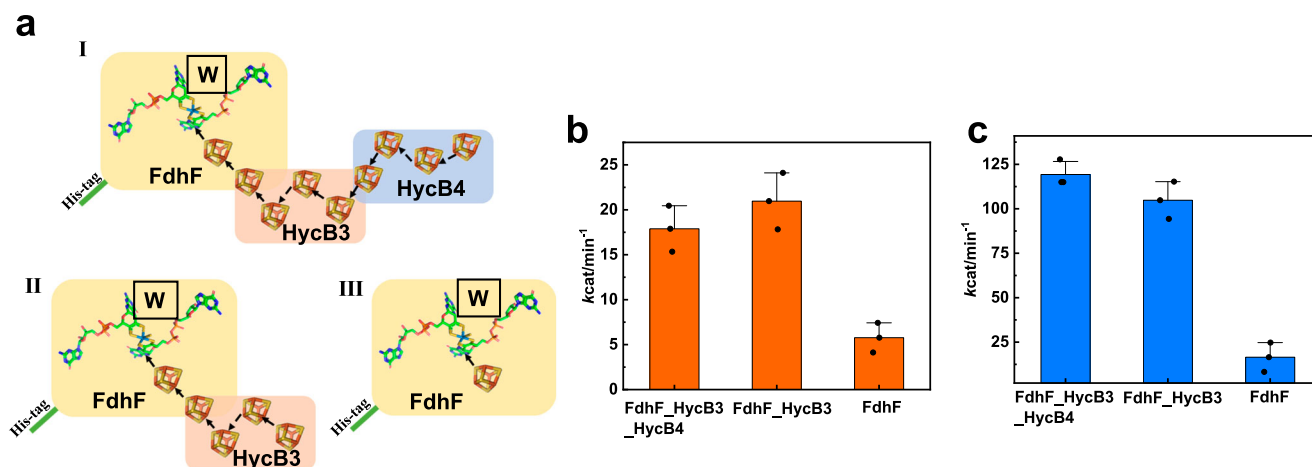


Fig. 3 | Truncation of *TkHDCR*. **a** Schematic models of three *TkHDCR* variants³⁸, (I) FdhF_HycB3_HycB4, (II) FdhF_HycB3, and (III) FdhF. **b** The turnover frequency of *TkHDCR* variants for formate oxidation. **c** The turnover frequency of *TkHDCR* variants for CO₂ reduction. The error bars correspond to the standard deviation of

at least three independent measurements, and the center value for the error bars is the average of the three independent measurements. Source data are provided as a Source Data file.

three variants, FdhF_HycB3_HycB4 (HDCRΔHydA2), FdhF_HycB3 (HDCRΔHydA2ΔHycB4), and FdhF (HDCRΔHydA2ΔHycB4ΔHycB3) (Fig. 3a and Supplementary Fig. 4a). The activity determination results indicate that FdhF_HycB3 and FdhF_HycB3_HycB4 exhibits equivalent activity in both the reduction of CO₂ and formate oxidation (Fig. 3b, c). However, FdhF's activity decreases by approximately 80% compared to FdhF_HycB3, suggesting that HycB3 is crucial as an electron transfer protein. The distal [Fe-S] cluster in HycB3 is likely helpful for electron shuffling between electron carriers and the metal active site (Supplementary Fig. 5). When one of its coordinated residues, C83, was substituted by serine (Supplementary Fig. 4b), the catalytic activity completely vanished. Compared to FdhF_HycB3_HycB4, FdhF_HycB3 has a smaller molecular weight, which may facilitate better fixation and transfer of electrons on the electrode. Therefore, FdhF_HycB3 was selected for further study.

It is noted that the activity of FdhF_HycB3 in reducing CO₂ was lower than that of *TkHDCR*, which may be attributed to self-aggregation and abnormal conformations. In the original *TkHDCR*, the formation of the nanowire structure relied on the crosslinking mediated by the highly similar C-terminal α -helical structures in HycB3 (sequences G159-K184, purple part in Fig. 4a) and HycB4 (sequences P190-R210)²⁵. FdhF_HycB3 may undergo self-aggregation via fragments 159–184, thereby decreasing its specific activity. Dynamic light scattering (DLS) measurements validate this hypothesis with a wide range of size distributions (Supplementary Fig. 6a). In addition, FdhF and HycB3 fail to adopt the correct conformation when HycB3 does not participate in the formation of nanowire. Structural analysis revealed that the FdhF subunit directly interacts with Helix 159–184 to form an incorrect conformation, resulting in an increase in the distance between the two [Fe-S] clusters in HycB3 and FdhF (from 11.3 Å to 30.7 Å) and disrupting the electron hopping between them (Supplementary Fig. 7a, b).

Based on these observations, a variant of FdhF_HycB3 was generated by removing the α -helix (G159-K184), namely, FdhF_HycB3Δ159–184 (Supplementary Fig. 4b and Fig. 4a). Activity determination, DLS and docking analysis of FdhF_HycB3Δ159–184 were also carried out. As a result, the catalytic activities partially improved to $553.7 \pm 122.4 \text{ min}^{-1}$ for CO₂ reduction and $400.8 \pm 85.8 \text{ min}^{-1}$ for formate oxidation (Fig. 4b). DLS analysis revealed an enhanced distribution below 50 nm, which approached the size of the monodispersed enzyme molecule (Supplementary Fig. 6b). In the structural modeling of HycB3Δ159–184, a conformation overlaying well with FdhF and

HycB3 in the PDB structure was observed (Supplementary Fig. 7c, d), confirming the adverse structural effect of the C-terminal α -helix of HycB3 on the variant FdhF_HycB3. In addition, we have performed elemental analysis (W) of FdhF_HycB3Δ159–184 using ICP-OES, which revealed 13.6 nmol of W was detected when the amount of protein is 16.6 nmol of protein. The above 80% of metal filling in enzyme molecules suggests the reliability of k_{cat} determination and the proper enzyme folding/maturation during heterologous expression in *E. coli*.

After obtaining the beneficial variant FdhF_HycB3Δ159–184, the temperature profile was determined since *TkHDCR* is a thermostable enzyme with the maximum catalytic activity at 70 °C¹². As shown in Fig. 4c, the activity of formate oxidation increases with the elevated temperature, reaching $1110.7 \pm 57.6 \text{ min}^{-1}$ at 70 °C. Meanwhile, the maximum CO₂ reduction activity reaches $1579.5 \pm 100.9 \text{ min}^{-1}$ at 60 °C and decreases to $774.4 \pm 129.7 \text{ min}^{-1}$ at 70 °C. The decreased reduction activity at 70 °C might be caused by partial enzyme inactivation. Similar behavior for the temperature-dependent activity of *DvFDH* was reported³⁹. This was further proved by the nonlinear fitting of the temperature-dependent model (Supplementary Fig. 8)⁴⁰.

Electrocatalytic characterization of FdhF_HycB3Δ159–184 electrode towards CO₂ reduction

The electrocatalysis of FdhF_HycB3Δ159–184 was characterized by constructing an FdhF_HycB3Δ159–184/carbon nanotube/glassy carbon electrode (FdhF_HycB3Δ159–184/CNT/GC). A cyclic voltammetric (CV) experiment of FdhF_HycB3Δ159–184/CNT/GC electrode was carried out upon adding an equal amount of formate and NaHCO₃. As shown in Supplementary Fig. 9, the reduction potential of CO₂ catalyzed by FdhF_HycB3Δ159–184/CNT/GC electrode vary from pH 6.2 to pH 8.0. Similar to that observed previously for *SfFDH*¹³ and *EcFDH-H*⁴⁴, the initial potential is $-410 \pm 2 \text{ mV vs. SHE}$ at pH 7.0, which is consistent with the formic acid /CO₂ redox potential (-412 mV vs. SHE) at pH 7.0¹³. The zero-current point (Net formate oxidation occurs at all potentials above the intersection, and net CO₂ reduction occurs at all potentials below it) represents the thermodynamic reduction potential for the CO₂/formate interconversion. The near-zero overpotential endows FdhF_HycB3Δ159–184 with superior performance to chemical catalysts for energy-saving direct CO₂ transformation⁴¹. While the onset of CO₂ reduction positively shifted to $-370 \pm 4 \text{ mV vs. SHE}$ at pH 6.2 and negatively shifted to $-471 \pm 3 \text{ mV vs. SHE}$ at pH 8.0. The decreased catalytic current for CO₂ reduction at pH 8.0 compared to

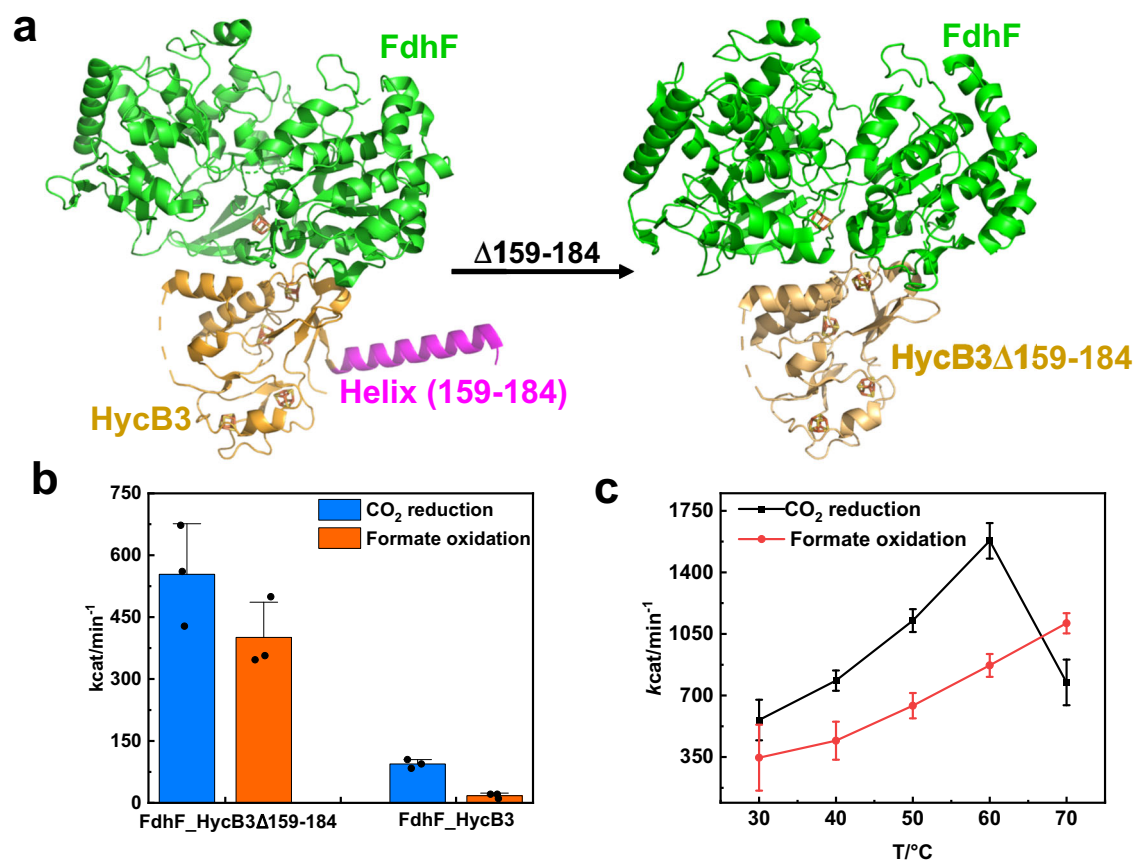


Fig. 4 | Rational design of FdhF_HycB3 for improved catalytic activity.

a Engineering strategy. **b** The turnover frequency of FdhF_HycB3 and FdhF_HycB3Δ159-184 toward formate oxidation and CO₂ reduction. **c** Temperature profile of FdhF_HycB3 Δ159-184 catalyzing formate oxidation and CO₂ reduction.

The error bars correspond to the standard deviation of at least three independent measurements, and the center value for the error bars is the average of the three independent measurements. Source data are provided as a Source Data file.

those at pH 6.2 and 7.0 might be caused by the accelerated CO₂ hydration in alkaline solutions²³. It has been previously reported that the CO₂ molecule, rather than its hydrated HCO₃⁻ and CO₃²⁻ species, is the substrate of formate dehydrogenases, so it is in the case of FdhF_HycB3Δ159-184⁴². The FdhF_HycB3Δ159-184/CNT/GC electrode was also tested in a CO₂-saturated electrolyte. The current density (the capacitance current doesn't participate in the calculation of the enzymatic turnover current) for CO₂ reduction reached $270.0 \pm 7.1 \mu\text{A cm}^{-2}$ at -550 mV vs. SHE (Fig. 5a and Table 1). Considering that the maximum catalytic activity of FdhF_HycB3Δ159-184 was observed at 60 °C, the electrocatalytic activity was also assessed at different temperatures. As shown in Fig. 5b, the catalytic current increases with the elevated temperature (from 30 °C to 60 °C), reaching $600.0 \pm 94.4 \mu\text{A cm}^{-2}$ at -550 mV vs. SHE at 60 °C. In mediated electron transfer (MET) mode, MV is supplemented in the electrolyte. As shown in Fig. 5c, the catalytic current reaches $800.0 \pm 83.1 \mu\text{A cm}^{-2}$ at -550 mV vs. SHE , which is 3 times greater than that in DET mode.

Mass transfer and kinetics of electrocatalysts are two main factors dominating electrocatalytic performance. To study the effect of mass transfer, a rotating disk electrode (RDE) was used. Figure 5d displays the LSVs of FdhF_HycB3Δ159-184/CNT/RDE obtained at different rotation rates (0, 100, and 900 rpm). Interestingly, no significant differences in current were observed with increasing rotation rate, suggesting that mass transfer has little influence on FdhF_HycB3Δ159-184 catalyzing the CO₂ reduction reaction and that the intrinsic enzymatic capability is the limiting factor, in accordance with the findings shown in Fig. 5b. To determine the kinetic parameters, a potential of -550 mV

vs. SHE was applied to FdhF_HycB3Δ159-184/CNT/GC and current were recorded at different concentrations (0–50 mM) of NaHCO₃, which was widely used for studying the kinetics of bioelectrodes in the context of CO₂ reduction^{10,18} (Fig. 5e), and according to Fig. 5e, the relationship between the current density and the substrate concentration was plotted in Fig. 5f. This result conforms to a typical Michaelis-Menten curve, with a calculated apparent *K_m* value of $0.7 \pm 0.1 \text{ mM CO}_2$. As the solubility of CO₂ at ambient temperature and pressure is $\sim 33 \text{ mM}$, which is much higher than the concentration needed for maximum catalysis (10 mM), these results explain why rotation fails to affect the electrocatalytic performance. This phenomenon is different from that of the electrocatalytic oxygen reduction reaction, in which mass transfer limitations exist in most cases because of the extremely low solubility of oxygen in aqueous solution (0.5 mM at 25 °C and 101.3 kPa)⁴³. To further illustrate the influence of FDH kinetics on electrocatalytic CO₂ reduction, two reported FDHs, FDH from *Cupriavidus necator* and FDH from *Rhodobacter aestuarii*, were tested. *CnFDH*⁴⁴ exhibited a moderate CO₂ reduction activity of 1.0 U mg^{-1} , and *RaFDH*³⁶ exhibited a low CO₂ reduction activity of 0.3 U mg^{-1} . As expected, slight catalytic currents were generated in both cases (Supplementary Fig. 10), demonstrating that the activity of FDH is still a determinant and that continuous enzyme design/engineering is necessary.

Electrocatalytic synthesis of formate from CO₂ at FdhF_HycB3Δ159-184 electrodes

Before constructing the electricity-driven formate synthesis system, the chemical energy-driven CO₂-formate conversion mode was

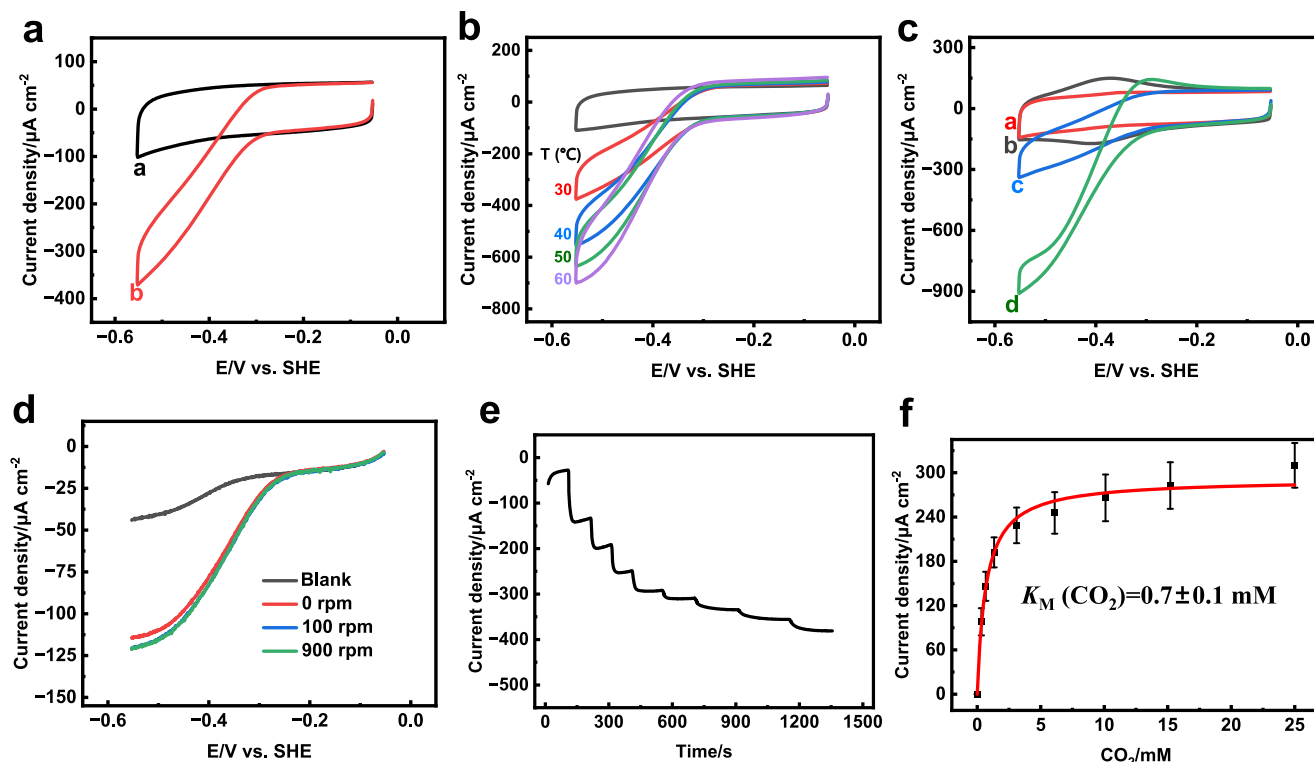


Fig. 5 | Electrochemical characterization of FdhF_HycB3Δ159-184/CNT/GC electrodes. **a** Cyclic voltammogram of FdhF_HycB3Δ159-184 for electrocatalytic CO₂ reduction; line a (black) was performed in 100% N₂, and line b (red) was performed in an atmosphere of CO₂ by bubbling CO₂ with a flow rate of 20 sccm. **b** Cyclic voltammogram of FdhF_HycB3Δ159-184 for electrocatalytic CO₂ reduction at different temperatures. The flow rate of CO₂ was 20 sccm. **c** Cyclic voltammogram of FdhF_HycB3Δ159-184 electrocatalytic analysis of direct and indirect electron transport, line a (red): FdhF_HycB3Δ159-184/CNT/GC electrode was evaluated in 100% N₂; line b (black): the electrode was evaluated in the presence of 0.2 mM methyl viologen (MV) and 100% N₂; line c (blue): the electrode was evaluated in 100% CO₂; line d (green): the electrode was evaluated in the presence of 0.2 mM MV and 100% CO₂. **d** Linear sweep voltammetry (LSV) at 0 rpm (red), 100 rpm (blue),

and 900 rpm (green) in an atmosphere of CO₂. **e** A potential of -550 mV *vs.* SHE was applied to FdhF_HycB3Δ159-184/CNT/GC for CO₂ reduction in mixed-buffer 0.1 M (Acetate, MES, HEPES, and TAPS), pH 6.0 buffer and NaHCO₃ (0–50 mM) was used as the substrate, 25 °C. **f** The catalytic currents and substrate concentrations are plotted. The experiments of (a), (b), (c), and (d) were carried out in 0.1 M HEPES, pH 6.2, buffer containing 0.1 M NaCl at 25 °C (excluding temperature optimization experiments), and at a scan rate of 5 mV s⁻¹ (LSV was conducted at a scan rate of 1 mV s⁻¹). HEPES: 4-(2-hydroxyethyl)-1-piperazineethanesulfonic acid, CNT: Carbon nanotubes. The error bars correspond to the standard deviation of at least three independent measurements, and the center value for the error bars is the average of the three independent measurements. Source data are provided as a Source Data file.

evaluated. With sodium dithionite (DTH) as the sacrificial reductant (electron donor) and MV as the electron mediator, 1.3 mM formate was detected after 1 h of aqueous catalysis (Supplementary Fig. 11a), validating the effectiveness of the FdhF_HycB3Δ159-184 variant and the feasibility of constructing an electricity-driven formate synthesis system. In DET mode (Fig. 6a and Supplementary Fig. 12a), -500 mV *vs.* SHE was applied for uninterrupted 14 h of electrolysis, and formate was generated as the sole product, as confirmed by HPLC (Supplementary Fig. 11b) and ¹H NMR (Supplementary Fig. 13). The yield of formate increases to 8.0 ± 0.5 mM in 14 h, with an average synthesis rate of 2.9 ± 0.2 μmol h⁻¹ cm⁻², which is higher than the rate of 1.42 μmol h⁻¹ cm⁻² catalyzed by conductive hydrogel-mediated C/FDH¹⁷. At 4 h, the system reached the maximum faradaic efficiency (FE%) and cathodic energy efficiency (CEE%) of 99.1% and 94.6%, respectively, and the synthesis rate of 5.8 μmol h⁻¹ cm⁻² (Fig. 6b). This high CEE is even greater than that of Bi-based catalysts, which have excellent selectivity (57%, 86%)^{45,46}, because of the high selectivity and near-zero overpotential of enzyme catalysis. In the MV-mediated mode (Fig. 6c and Supplementary Fig. 12b), formate accumulated rapidly in the 6 hours and then became moderate, probably because of the poor electrode stability, until it reached 22.8 ± 1.6 mM at 16 h. The average production rate is as high as 7.1 ± 0.5 μmol h⁻¹ cm⁻². At 6 h, the system reached the maximum FE% and CEE% of 98.9% and 94.4%, respectively, and the synthesis rate of 15.2 ± 0.6 μmol h⁻¹ cm⁻² (Fig. 6d). This rate is lower than the best formate production rate of

55 μmol h⁻¹ cm⁻² reported by Reisner et al.²¹, but it is higher than most bioelectrodes used for the electrocatalytic synthesis of formic acid (Table 1). Further optimization of immobilization strategies could improve the formic acid production efficiency of this system.

In the present work, we achieved convenient and efficient heterologous expression of *TkHDCR* by *E. coli*, grounding enzyme engineering for an electro-responsive carbon dioxide reductase and its massive production. The engineering of *TkHDCR* by subunit truncation and rational design revealed that the HycB3 subunit is essential for electron shuffling, while its original “arm”, helix 159-184, is harmful for enzyme molecule dispersion and proper conformation preservation. Thus, FdhF_HycB3Δ159-184 was generated, with a maximum specific activity of 1579.5 min⁻¹ at 60 °C. The electrocatalytic determination of FdhF_HycB3Δ159-184 demonstrated DET-type bioelectrocatalysis. The catalytic current in the MET mode is ~3 times greater than that in the DET mode. Since the distal Fe-S cluster of HycB3 facilitates electron transfer between HycB3 and FdhF, immobilizing HycB3 in a specific orientation on the electrode might improve direct electron transfer. Since the *K_m* value is calculated as 0.7 ± 0.1 mM CO₂, which is much lower than the solubility of CO₂, mass transfer is not the rate-limiting factor. By applying an applied voltage to the MV-mediated FdhF_HycB3Δ159-184 electrode for CO₂ transformation, a formate concentration of 22.8 ± 1.6 mM and a yield rate of 7.1 ± 0.5 μmol h⁻¹ cm⁻² were observed after 16 hours. An FE of 98.9% and a CEE of 94.4% were attained. This demonstrates the potential of FdhF_HycB3Δ159-184 as a

catalyst for environmentally friendly and sustainable formate production. Some fixation strategies may further improve the stability and efficiency of FdhF_HycB3Δ159-184 bioelectrode. Moreover, the generated formate holds promise for conversion into higher-value commodities through enzymatic catalysis.

Methods

Reagents and materials

All the chemicals were of analytical grade or of higher purity and were purchased from Sigma–Aldrich, Macklin (Shanghai, China), and Sino-pharm (Beijing, China) unless otherwise noted. Primers and genes were synthesized by Tsingke (Beijing, China), and Primers were dissolved in Milli-Q water to a final concentration of 10 μM. PrimeSTAR Max DNA Polymerase was obtained from Takara Bio (Japan). The methylation-sensitive restriction enzyme (*DpnI*) was obtained from New England Biolabs. A ClonExpress-II one-step cloning kit was obtained from Vazyme (Nanjing, China). Lysogeny Broth (LB) medium (1 L) containing 10 g of NaCl, 10 g of tryptone and 5 g of yeast extract. For the LB agar plates, 20 g of agar was added. All the media were then autoclaved at 121 °C for 20 min. For the anaerobic culture medium, 100 mM 3-(N-morpholino) propanesulfonic acid (MOPS), 5 g L⁻¹ glucose, 25 mM sodium fumarate, and 1 mg L⁻¹ resazurin were added to LB media, and the pH was adjusted to 7.4. The anaerobic culture medium was autoclaved at 115 °C for 30 min, after which the oxygen was replaced with 100% N₂. Carbon nanotubes (CNTs) were obtained from XFNANO (Nanjing, China).

Construction of plasmids

The *hdcR* gene was codon optimized and synthesized and subsequently cloned and inserted into pET20b by Tsingke. The polymerase chain reaction (PCR) mixture (50 μL) consisted of 25 μL of PrimeSTAR Max DNA Polymerase, 20 ng of the template (pET20b-*hdcR*), and 500 nM primers P1 and P3, followed by the PCR protocol: 98 °C for 2 min (1 cycle); 98 °C for 20 s; 53 °C for 20 s; 72 °C for 2 min (25 cycles); and 72 °C for 10 min (1 cycle). PCR products were characterized by agarose gel electrophoresis. The Megawhop PCR mixture (50 μL) contained 25 μL of PrimeSTAR Max DNA Polymerase, 20 ng of the pTrcHisA plasmid as the template, and 500 nM primers P2 and P4. The PCR protocol was as follows: 98 °C for 2 min (1 cycle); 98 °C for 30 s, 53 °C for 20 s, and 72 °C for 2 min (25 cycles); and 72 °C for 10 min (1 cycle). All the methylated templates were specifically degraded by *DpnI*. The PCR products were purified with a universal DNA purification and recovery kit (TIANGEN, China, Beijing). The above two PCR products were linked with a ClonExpress-II one-step cloning kit (37 °C, 30 min). The linked product was subsequently transformed into 100 μL of *E. coli* Top10 competent cells (heated at 42 °C for 45 sec) and recovered at 37 °C for 1 h. The cells were subsequently plated on LB agar plates supplemented with 50 mg L⁻¹ ampicillin for growth overnight at 37 °C.

The construction of the plasmid pTrc99a was performed with kanamycin resistance. The kanamycin resistance gene was cloned from the template pET28a using the primers P11 and P12. pTrc99a was generated by removing the original ampicillin resistance gene via the primers P13 and P14, and the pTrc99a-kan⁺ plasmid harboring the kanamycin resistance gene was generated via the ClonExpress-II one-step cloning kit. The linked product was subsequently transformed into 100 μL of *E. coli* Top10 competent cells, which were subsequently allowed to recover at 37 °C for 1 h. The cells were plated on LB agar plates supplemented with 50 mg L⁻¹ kanamycin for growth overnight at 37 °C.

The plasmid pTrc99a-kan⁺-*hydGXEF* containing the maturation factor genes *hydG*, *hydX*, *hydE*, and *hydF* of FeFe-hydrogenase from *Shewanella oneidensis* MR-1 was constructed using the primers P15, P16, P17 and P18. pTrc99a-kan⁺-*hydGXEF* and pTrcHisA-*hdcR* were subsequently transformed into *E. coli* MC1061 competent cells. The

Table 1 | Comparison of electrocatalytic CO₂ reduction by Mo/W-containing FDHs

Enzymes	Electrode modification	Electron transfer types	Potential/V vs. SHE	Current density /μA cm ⁻² (mA cm ⁻²)	Concentration of formate/mM	Electrode area/cm ²	Production rate/μmol h ⁻¹ cm ⁻²	Reference
SFDH-1	Pyrolytic graphite electrode	DET	-0.8	-80	-	-	-	13
EcFDH	Pyrolytic graphite electrode	DET	-0.6	-200	-	-	-	14
CIFDH	Pyrolytic graphite electrode	DET	-0.8	-400	-	-	-	16
CIFDH	Conductive polyaniline (PANI) hydrogel	MET	-0.4	-	-	1.0	1.42	17
EcFDH	Grafted to poly(allylamine) modified carbon electrode	MET	-0.66	-62	-	0.8	0.4	18
DvH-FDH	4-nitrophenyl radical-modified graphite electrode	DET	-0.7	-200	0.004	0.2	0.44	19
DvH-FDH	MesoTiO ₂ electrode	DET	-0.6	-100	4.9	0.25	0.82	48
DvH-FDH	IO-TiO ₂ Perovskite BiVO ₄	DET	-	(-5)	-	0.19	7	49
DvH-FDH	Mesoporous indium-tin-oxide	DET	-0.8	(-3.6)	-	0.19	55	21
DvH-FDH	NHMe ₂ ⁺ modified carbon nanotubes	DET	-0.6	-247	1.98	0.07	1.2	20
DvH-FDH	MET	MET	-0.6	-	4.18	0.07	2.5	20
FdhF_HycB3Δ159-184	Carbon nanotubes	DET	-0.5	-270	8.0	1.0	2.9	This study
		MET	-0.5	-800	22.8	1.0	7.1	This study

DET: Directed electron transfer. MET: Mediated electron transfer.

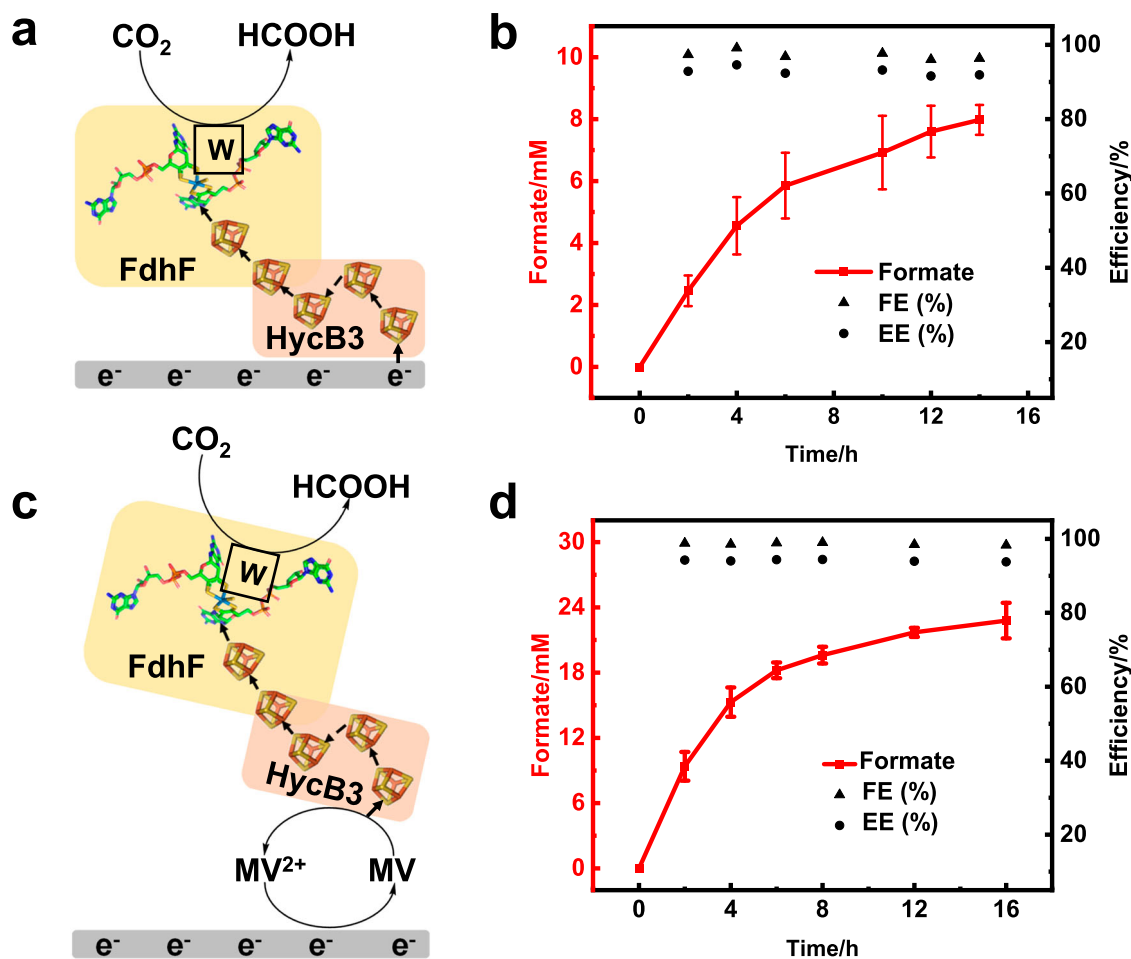


Fig. 6 | Electrosynthesis of formate from CO₂ at FdhF_HycB3Δ159-184 electrodes. **a** Electrocatalysis via direct electron transfer; **(b)** formate produced by electrocatalysis via direct electron transfer; **(c)** electrocatalysis via mediated electron transfer by adding 0.2 mM MV into the electrolyte; **(d)** formate produced by electrocatalysis via mediated electron transfer. Electrolyte: 0.1 M HEPES/NaOH, 0.1 M

NaCl buffer, pH 7.0. A constant voltage of -500 mV vs. SHE was used. The error bars correspond to the standard deviation of at least three independent measurements, and the center value for the error bars is the average of the three independent measurements. Source data are provided as a Source Data file.

clone was picked from LB agar plates containing kanamycin and ampicillin. *E. coli* MC1061 containing pTrc99a-kan⁺-*hydGXEF* and pTrcHisA-*hdcr* was used to express HDCR. The pTrcHisA-*fdhF_hycB3_hycB4* (pTrcHisA-*hdcrΔhydA2*), pTrcHisA-*fdhF_hycB3* (pTrcHisA-*hdcrΔhydA2ΔhycB4*), and pTrcHisA-*fdhF* (pTrcHisA-*hdcrΔhydA2ΔhycB4ΔhycB3*) were constructed using primers P5 and P6, P5 and P7, and P5 and P8, respectively. The plasmid was transformed into *E. coli* MC1061 competent cells. The clone was picked from the LB agar plates containing ampicillin. The FdhF_HycB3Δ159-184 variant-expressing plasmid pTrcHisA-*fdhF_hycB3Δ159-184* (pTrcHisA-*hdcrΔhydA2ΔhycB4Δ159-184*) was constructed by using pTrcHisA-*fdhF_hycB3* as a template, and using primer P9 and P10. The variant FdhF_HycB3-C83S expression plasmid was constructed by using primer P38 and P39, and pTrcHisA-*fdhF_hycB3* was used as the template.

The plasmid pETDuet-*hdcr* was constructed by cloning *fdhF* and *hycB3* into multiple cloning sites 1 (MCS1) of pETDuet-1 using P19 and P20, P21 and P22. The *hycB4* and *hydA2* genes were subsequently cloned and inserted into the MCS2 of pETDuet-1 using P23 and P24, P25, and P26. The maturation factor gene FdhD of FdhF was also cloned and inserted into MCS1 of pETDuet-1 using P20, P27, P28, and P29. In addition, the pACYCDuet-*hydGXEF* plasmid, which contains the maturation factor genes *hydG*, *hydX*, *hydE*, and *hydF* of FeFe-hydrogenase from *Shewanella oneidensis* MR-1, was constructed by cloning the *hydG* and *hydX* genes into the MCS1 of pACYCDuet-1 using

P30 and P31, P32 and P33, and cloning *hydE* and *hydF* into the MCS2 of pACYCDuet-1 using primers P34 and P35, P36 and P37. Both pETDuet-*hdcr* and pACYCDuet-*hydGXEF* were transformed together into *E. coli* BL21 (DE3) competent cells. The clone was picked from LB agar plates containing ampicillin and chloramphenicol. For primer sequences, please refer to Supplementary Table 1.

Protein expression and purification

For the expression of HDCR in *E. coli* BL21 (DE3), cells were grown anaerobically in anaerobic culture medium²⁹ supplemented with ampicillin (50 mg L⁻¹), chloramphenicol (30 mg L⁻¹), and 1 mM sodium tungstate. Cultures were grown anaerobically at 37 °C to an OD₆₀₀ of 0.6–0.8, 2 mM FeSO₄, and 0.4 g L⁻¹ L-cysteine were added. A final concentration of 0.2 mM isopropyl beta-D-1-thiogalactopyranoside (IPTG) was used for the induction of protein production for 20 h under anaerobic conditions at 18 °C and 150 rpm. For the expression of HDCR in *E. coli* MC1061, the conditions were the same as above, except for the change from ampicillin (50 mg L⁻¹) or chloramphenicol (30 mg L⁻¹) to ampicillin (50 mg L⁻¹) and kanamycin (50 mg L⁻¹). The expression of the HDCR variants in *E. coli* MC1061 was performed under the same conditions but with only the addition of ampicillin (50 mg L⁻¹).

All purification steps were performed under strictly anaerobic conditions at room temperature in an anaerobic chamber (Vigor Gas Purification Technologies Company, China Suzhou) filled with 96–98%

N₂ and 2–4% H₂, and an oxygen content below 2 ppm. For HDCR purification, cultures were centrifuged at 4 °C for 10 min at 4500 × *g*, resuspended in 30 mL of buffer A (25 mM Tris, 20% [v/v] glycerol, 20 mM MgSO₄, pH 7.5, and 1 mg L⁻¹ resazurin), centrifuged again and resuspended in buffer A supplemented with 40 mg L⁻¹ PMSF, 0.1 g L⁻¹ DNaseI, 2 g L⁻¹ lysozyme, and 0.5 mM dithiothreitol, and then incubated at 37 °C for 1 h. The cells are completely broken up by freezing and thawing three times with liquid nitrogen. Cell debris was removed by centrifugation at 17500 × *g* and 4 °C for 30 min. The cleared lysate was added to 3 mL of Ni-nitrilotriacetate (Ni-NTA), which was equilibrated with 15 mL of buffer A containing 40 mg L⁻¹ PMSF and 0.5 mM dithiothreitol. The resin was subsequently washed with 25 column volumes of buffer A containing 40 mM imidazole, 40 mg L⁻¹ PMSF, and 0.5 mM dithiothreitol, and the retained protein was eluted with ~5 mL of the same buffer A containing 250 mM imidazole, 40 mg L⁻¹ PMSF and 2 mM dithiothreitol. For the purification of the other HDCR variants, buffer B (100 mM Tris, 100 mM NaCl, 10 mM NaNO₃, pH 8.0, and 1 mg L⁻¹ resazurin) was used, and the purification procedure was the same as above. The protein purifier (AKTA purifier 10) equipped with Superdex 200 (10/300 GL, General Electric Company) was used for further purification. The flow of buffer was 0.9 mL min⁻¹. The protein concentration was measured according to the Bradford method. The proteins were separated on 15% polyacrylamide gels and stained with Coomassie brilliant blue G250.

Enzyme activity assay

Enzyme activity assays were performed in an anaerobic chamber. Buffer C (HEPES/NaOH 100 mM, 20 mM MgSO₄, pH 7.0, 2 mM DTT) was used for HDCR, buffer D (HEPES/NaOH 100 mM, pH 7.0, 2 mM DTT) was used for HDCR variants, and DTT was used as the protective reagent for enzymes. For formate oxidation, 20 mM substrate, sodium formate, and 20 mM electron acceptor, MV²⁺, were added into Buffer C/D, and the total volume was 2 mL. The absorption at 604 nm ($\epsilon = 13.9 \text{ mM}^{-1} \text{ cm}^{-1}$), assigned to the reduced MV⁺, was monitored by Evolution One (Thermo Fisher Scientific) with a temperature control module after the addition of HDCR and its variants. One unit of oxidation activity was defined as oxidizing 1 μmol of formate (reducing 2 μmol of MV²⁺) per minute under the assay conditions.

For CO₂ reduction, MV was first reduced by sodium dithionite (DTH) to produce the reduced MV, which is used as the electron donor for CO₂ reduction. Similarly, the absorption decreased at 604 nm ($\epsilon = 13.9 \text{ mM}^{-1} \text{ cm}^{-1}$), and Evolution One (Thermo Fisher Scientific) was monitored with a temperature control module after the addition of HDCR and its variants. One unit of reduction activity was defined as reducing 1 μmol of CO₂ (oxidizing 2 μmol of MV⁺) per minute under the assay conditions.

For a temperature-dependent experiment, the temperature is controlled by a water bath and temperature-controlling module in a UV-Vis spectrophotometer (Evolution One, Thermo Fisher Scientific). Enzyme aliquots were stored in a water bath at a specific temperature for 10 min, and the pre-mixed reaction buffer without enzyme was incubated inside the spectrophotometer with the temperature module controlled via the software.

Enzyme catalytic CO₂ reduction in solution

The enzyme catalytic reaction was performed in an anaerobic chamber. 20 mM of reduced MV was used as the electron donor, CO₂ was used as the substrate, and 50 μg of FdhF_HycB3 Δ 159–184 was used as the catalyst in 5 mL of the reaction solution. The control used inactive FdhF_HycB3 Δ 159–184, which was prepared by boiling for 20 min. After 1.5 h at 30 °C, 100 μL samples were taken, and 5 mM sulfuric acid was added to stop the reaction. The samples were centrifuged at 12000 × *g* for 10 min, and the produced formic acid was detected by high-performance liquid chromatography (HPLC) equipped with a RID–20A detector (Nexera XR, Shimadzu) and an Aminex HPX-87H column

(300 × 7.8 mm, Bio-Rad). The mobile phase was 5 mM sulfuric acid, the flow rate was 0.6 mL min⁻¹, and the column temperature was 60 °C.

Electrochemical experiments

Electrochemical measurements were carried out using a potentiostat (CHI660e) and a rotating disk electrode (PINE) in the anaerobic chamber with 100% N₂. A three-electrode system was used. The glassy carbon electrodes (0.07 cm²) were polished with an alumina slurry (0.05 μm) on a polishing cloth and then sonicated for 1 min in deionized water and ethanol, respectively. A homogenous black CNT was dispersed in water and dimethylformamide (DMF) (ratio of 1:1) to a concentration of 1 g L⁻¹. A 10 μL aliquot of the CNT suspension was drop-cast on a fresh GC electrode, denoted as the CNT/GC electrode. For the bioelectrode, 10 μL of enzyme (1 g L⁻¹) was drop-cast on the CNT/GC electrode and then left to stand at 4 °C for 4 h in an anaerobic chamber. The excess enzyme solution was gently washed off before testing. A platinum wire was used as the counter electrode, and a saturated Ag/AgCl electrode was used as the reference electrode. All applied potentials were converted versus the standard hydrogen electrode (SHE) using the following equation 1 at 25 °C and pH 7.0.

$$ESHE = E_{Ag/AgCl} + 197mV \quad (1)$$

Cyclic voltammetry (CV) and linear sweep voltammetry (LSV) analyses were performed at 25 °C in 100 mM HEPES/NaOH and 100 mM NaCl at pH 7.0. In the pH-dependence experiment, pH was controlled by using a mixed-buffer system [100 mM Acetate, 2-morpholinoethane sulfonic acid (MES), *N*-cyclohexyl-2 aminoethane sulfonic acid (HEPES), and *N*-tris(hydroxymethyl)methyl-3-aminopropanesulfonic acid (TAPS)], and checked following experimentation. The electrode speed was 900 rpm, the scan rate was 5 mV s⁻¹ for CV, and the scan rate was 1 mV s⁻¹ for LSV. The electrolytic cell with a heating layer was used for the temperature optimization experiment. The temperature of the pool is controlled by a flowing water bath, and cyclic voltammetry is performed after reaching the desired temperature, as confirmed by a thermometer test.

Enzyme-electrocatalytic CO₂ reduction to formate

A carbon paper (TORAY, Japan) with an area of 1 cm² was used as the supporting enzyme, 100 μL of CNTs (1 g L⁻¹) was added to the carbon paper, and after drying, 95 μL of FdhF_HycB3 Δ 159–184 solution (1 g L⁻¹) and 5 μL of Nafion (0.02%) were mixed and added to the CNTs to build FdhF_HycB3 Δ 159–184/carbon nanotube/carbon paper (FdhF_HycB3 Δ 159–184/CNT/CP) electrode, after which the mixture was allowed to stand at 4 °C for 4 h in an anaerobic chamber. The excess enzyme solution was gently removed. A three-electrode electrochemical cell with FdhF_HycB3 Δ 159–184/CNT/CP electrode as the working electrode, Ag/AgCl electrode as the reference electrode, and platinum sheet (1 cm²) as the counter electrode was used. Chronoamperometry was carried out in 5 mL of buffer (100 mM HEPES/NaOH, 100 mM NaCl, pH 7.0) that was continuously fed pure CO₂, and a constant voltage of –0.5 V vs. SHE was used. For the MET enzyme-electrocatalytic CO₂ reduction to formate, 0.2 mM MV was added to the electrolyte. The formate concentration in the electrolyte was detected by a high-performance liquid chromatography (HPLC) instrument equipped with a RID-20A detector (Nexera XR, Shimadzu) and an Aminex HPX-87H column (300 × 7.8 mm, Bio-Rad). The samples were prepared by adding H₂SO₄ at a final concentration of 5 mM and were centrifuged for 10 min at 12000 × *g*. The mobile phase was 5 mM sulfuric acid, the flow rate was 0.6 mL min⁻¹, and the column temperature was 60 °C. The standard curve for formate was generated by employing known concentrations of formate ranging from 1 to 100 mM. For the ¹H-NMR experiment, 400 μL of electrolyte and 200 μL of D₂O were mixed in a clean NMR tube and subsequently

analyzed via one-dimensional ^1H liquid NMR spectroscopy (Bruker Advance 600 MHz). The faraday efficiency (FE) and half-cell cathodic energy efficiency (CEE%) of formate were calculated according to Eqs. 2 and 3⁴⁶.

$$FE(\%) = \frac{Q(\text{formate})}{Q(\text{tot})} * 100\% = \frac{c(\text{formate}) * V * z * F}{j * t} \quad (2)$$

where c (formate) is the formate concentration after reaction time t (s), V is the volume of the electrolyte, z is the number of electrons required to reduce CO_2 to formate, and the value is 2, F is the Faraday constant ($96,485 \text{ C mol}^{-1}$), and j is the recorded current.

$$CEE(\%) = \frac{1.23 - E(\text{formate})}{1.23 - E(\text{applied})} * FE * 100\% \quad (3)$$

where E (formate) = -0.42 V vs. SHE is the reduction potential of CO_2 reduction to formate at pH 7.0. FE is the faradaic efficiency of formate production. E (applied) = -0.5 V vs. SHE is the applied potential vs. SHE.

Dynamic light-scattering assay

A NanoBrook 90plus instrument (Brookhaven Instruments Corporation, USA) was used to analyze the particle size of the proteins. The concentration of all the samples was 0.5 g L^{-1} and the samples were centrifuged for 10 min at $12000 \times g$ and 4°C . Each measurement was made three times at 25°C .

ICP-OES analysis

The W element in FdhF_HycB3Δ159-184 was analyzed through ICP-OES (Thermo, ICPOES7200) by Beijing Zhongke Baice Technology Service Co., Ltd.

Bioinformatic methods

All DNA sequences were retrieved from the National Center for Biotechnology Information database, and all protein structures were obtained from the Protein Data Bank. The plasmid map was generated by SnapGene, and the protein structures were visualized using PyMOL. Protein docking analysis was performed via ZDOCK⁴⁷.

Reporting summary

Further information on research design is available in the Nature Portfolio Reporting Summary linked to this article.

Data availability

Data supporting the findings of this work are available within the paper and its Supplementary Information files. A reporting summary for this Article is available as a Supplementary Information file. Source data are provided in this paper.

References

- Liu, Z., Wang, K., Chen, Y., Tan, T. & Nielsen, J. Third-generation biorefineries as the means to produce fuels and chemicals from CO_2 . *Nat. Catal.* **3**, 274–288 (2020).
- Li, L., Li, X., Sun, Y. & Xie, Y. Rational design of electrocatalytic carbon dioxide reduction for a zero-carbon network. *Chem. Soc. Rev.* **51**, 1234–1252 (2022).
- Fang, W. et al. Durable CO_2 conversion in the proton-exchange membrane system. *Nature* **626**, 86–91 (2024).
- Huang, J. E. et al. CO_2 electrolysis to multicarbon products in strong acid. *Science* **372**, 1074–1078 (2021).
- Xie, Y. et al. High carbon utilization in CO_2 reduction to multi-carbon products in acidic media. *Nat. Catal.* **5**, 564–570 (2022).
- Yang, Y. et al. Operando studies reveal active Cu nanograins for CO_2 electroreduction. *Nature* **614**, 262–269 (2023).
- Zhang, Y.-H. P. J., Zhu, Z., You, C., Zhang, L. & Liu, K. In vitro bio-transformation (ivBT): definitions, opportunities, and challenges. *Synth. Biol. Eng.* **1**, 10013 (2023).
- Nielsen, C. F., Lange, L. & Meyer, A. S. Classification and enzyme kinetics of formate dehydrogenases for biomanufacturing via CO_2 utilization. *Biotechnol. Adv.* **37**, 107408 (2019).
- Moon, M., Park, G. W., Lee, J., Lee, J.-S. & Min, K. Recent progress in formate dehydrogenase (FDH) as a non-photosynthetic CO_2 utilizing enzyme: A short review. *J. CO2 Util.* **42**, 101353 (2020).
- Sahin, S. et al. Bioelectrocatalytic CO_2 reduction by Mo-dependent formylmethanofuran dehydrogenase. *Angew. Chem. Int. Ed.* **62**, e202311981 (2023).
- Schuchmann, K. & Muller, V. Direct and reversible hydrogenation of CO_2 to formate by a bacterial carbon dioxide reductase. *Science* **342**, 1382–1385 (2013).
- Schwarz, F. M., Schuchmann, K. & Muller, V. Hydrogenation of CO_2 at ambient pressure catalyzed by a highly active thermostable biocatalyst. *Biotechnol. Biofuels* **11**, 237 (2018).
- Reda, T., Plugge, C. M., Abram, N. J. & Hirst, J. Reversible inter-conversion of carbon dioxide and formate by an electroactive enzyme. *Proc. Natl. Acad. Sci. USA* **105**, 10654–10658 (2008).
- Bassegoda, A., Madden, C., Wakerley, D. W., Reisner, E. & Hirst, J. Reversible interconversion of CO_2 and formate by a molybdenum-containing formate dehydrogenase. *J. Am. Chem. Soc.* **136**, 15473–15476 (2014).
- Robinson, W. E., Bassegoda, A., Reisner, E. & Hirst, J. Oxidation-state-dependent binding properties of the active site in a Mo-containing formate dehydrogenase. *J. Am. Chem. Soc.* **139**, 9927–9936 (2017).
- Li, W. et al. Direct detection of a single [4Fe-4S] cluster in a tungsten-containing enzyme: Electrochemical conversion of CO_2 into formate by formate dehydrogenase. *Carbon Energy* **5**, <https://doi.org/10.1002/cey2.304> (2023).
- Kuk, S. K. et al. NADH-free electroenzymatic reduction of CO_2 by conductive hydrogel-conjugated formate dehydrogenase. *ACS Catal.* **9**, 5584–5589 (2019).
- Yuan, M. et al. Creating a low-potential redox polymer for efficient electroenzymatic CO_2 reduction. *Angew. Chem. Int. Ed.* **130**, 6692–6696 (2018).
- Alvarez-Malmagro, J. et al. Bioelectrocatalytic activity of W-formate dehydrogenase covalently immobilized on functionalized gold and graphite electrodes. *ACS Appl. Mater. Interfaces* **13**, 11891–11900 (2021).
- Badiani, V. M. et al. Engineering electro- and photocatalytic carbon materials for CO_2 reduction by formate dehydrogenase. *J. Am. Chem. Soc.* **144**, 14207–14216 (2022).
- Edwardes Moore, E. et al. Understanding the local chemical environment of bioelectrocatalysis. *Proc. Natl. Acad. Sci. USA* **119**, e2114097119 (2022).
- Cobb, S. J., Rodríguez-Jiménez, S. & Reisner, E. Connecting biological and synthetic approaches for electrocatalytic CO_2 reduction. *Angew. Chem. Int. Ed.* **63**, e202310547 (2024).
- Cobb, S. J., Dharani, A. M., Oliveira, A. R., Pereira, I. A. C. & Reisner, E. Carboxysome-inspired electrocatalysis using enzymes for the reduction of CO_2 at low concentrations. *Angew. Chem. Int. Ed.* **62**, e202218782 (2023).
- Cobb, S. J. et al. Fast CO_2 hydration kinetics impair heterogeneous but improve enzymatic CO_2 reduction catalysis. *Nat. Chem.* **14**, 417–424 (2022).
- Dietrich, H. M. et al. Membrane-anchored HDCR nanowires drive hydrogen-powered CO_2 fixation. *Nature* **607**, 823–830 (2022).
- Hartmann, T., Schwanhold, N. & Leimkühler, S. Assembly and catalysis of molybdenum or tungsten-containing formate dehydrogenases from bacteria. *Biochim. Biophys. Acta Proteins Proteom.* **1854**, 1090–1100 (2015).

27. Niks, D. & Hille, R. Molybdenum- and tungsten-containing formate dehydrogenases and formylmethanofuran dehydrogenases: Structure, mechanism, and cofactor insertion. *Protein Sci.* **28**, 111–122 (2018).
28. Schlindwein, C., Giordano, G., Santini, C. L. & Mandrand, M. A. Identification and expression of the *Escherichia coli* fdhD and fdhE genes, which are involved in the formation of respiratory formate dehydrogenase. *J. Bacteriol.* **172**, 6112–6121 (1990).
29. Leo, F., Schwarz, F. M., Schuchmann, K. & Müller, V. Capture of carbon dioxide and hydrogen by engineered *Escherichia coli*: hydrogen-dependent CO₂ reduction to formate. *Appl. Microbiol. Biotechnol.* **105**, 5861–5872 (2021).
30. Thomé, R. et al. A sulfurtransferase is essential for activity of formate dehydrogenases in *Escherichia coli*. *J. Biol. Chem.* **287**, 4671–4678 (2012).
31. Arnoux, P. et al. Sulphur shuttling across a chaperone during molybdenum cofactor maturation. *Nat. Commun.* **6**, 6148 (2015).
32. Mulder, D. W. et al. Stepwise [FeFe]-hydrogenase H-cluster assembly revealed in the structure of HydAΔEFG. *Nature* **465**, 248–251 (2010).
33. Britt, R. D., Rao, G. & Tao, L. Biosynthesis of the catalytic H-cluster of [FeFe] hydrogenase: the roles of the Fe–S maturase proteins HydE, HydF, and HydG. *Chem. Sci.* **11**, 10313–10323 (2020).
34. Britt, R. D., Rao, G. & Tao, L. Bioassembly of complex iron–sulfur enzymes: hydrogenases and nitrogenases. *Nat. Rev. Chem.* **4**, 542–549 (2020).
35. Tyagi, A. K. et al. High-yield expression of heterologous [FeFe] hydrogenases in *Escherichia coli*. *PLoS ONE* **5**, e15491 (2010).
36. Min, K. et al. Elevated conversion of CO₂ to versatile formate by a newly discovered formate dehydrogenase from *Rhodobacter aes-tuarii*. *Bioresour. Technol.* **305**, 123155 (2020).
37. Ebrahimpour, A., Rahman, R. N. Z. R. A., Basri, M. & Salleh, A. B. High level expression and characterization of a novel thermostable, organic solvent tolerant, 1,3-regioselective lipase from *Geobacillus* sp. strain ARM. *Bioresour. Technol.* **102**, 6972–6981 (2011).
38. Dietrich, H. M. & Müller, V. Ferredoxin as a physiological electron donor for carbon dioxide fixation to formate in a bacterial carbon dioxide reductase. *ACS Catal.* **13**, 12374–12382 (2023).
39. Cobb, S. J. et al. A photoelectrochemical-thermoelectric device for semi-artificial CO₂ fixation employing full solar spectrum utilization. *Device* 100505, <https://doi.org/10.1016/j.device.2024.100505> (2024).
40. Wojcik, M. & Mitek, J. A new method to determine optimum temperature and activation energies for enzymatic reactions. *Bioprocess Biosyst. Eng.* **39**, 1319–1323 (2016).
41. Yang, J. Y., Kerr, T. A., Wang, X. S. & Barlow, J. M. Reducing CO₂ to HCO₂⁻ at mild potentials: lessons from formate dehydrogenase. *J. Am. Chem. Soc.* **142**, 19438–19445 (2020).
42. Meneghello, M. et al. Formate dehydrogenases reduce CO₂ rather than HCO₃⁻: An electrochemical demonstration. *Angew. Chem. Int. Ed.* **60**, 9964–9967 (2021).
43. Parkhill, K. L. & Gulliver, J. S. Indirect measurement of oxygen solubility. *Water Res.* **31**, 2564–2572 (1997).
44. Yu, X., Niks, D., Mulchandani, A. & Hille, R. Efficient reduction of CO₂ by the molybdenum-containing formate dehydrogenase from *Cupriavidus necator* (*Ralstonia eutropha*). *J. Biol. Chem.* **292**, 16872–16879 (2017).
45. Chang, S., Xuan, Y., Duan, J. & Zhang, K. High-performance electroreduction CO₂ to formate at Bi/Nafion interface. *Appl. Catal. B* **306**, 121135 (2022).
46. Li, Y. et al. Enhancing local CO₂ adsorption by L-histidine incorporation for selective formate production over the wide potential window. *Angew. Chem. Int. Ed.* **62**, e202313522 (2023).
47. Zhang, W., Meng, Q. Z., Tang, J. J. & Guo, F. Exploring effectiveness of ab-initio protein-protein docking methods on a novel anti-bacterial protein complex dataset. *Brief. Bioinform.* **22**, 13 (2021).
48. Miller, M. et al. Interfacing Formate dehydrogenase with metal oxides for the reversible electrocatalysis and solar-driven reduction of carbon dioxide. *Angew. Chem. Int. Ed.* **58**, 4601–4605 (2019).
49. Edwardes Moore, E. et al. A semi-artificial photoelectrochemical tandem leaf with a CO₂-to-formate efficiency approaching 1%. *Angew. Chem. Int. Ed. Engl.* **60**, 26303–26307 (2021).

Acknowledgements

This study was supported by Tianjin Synthetic Biotechnology Innovation Capacity Improvement Projects (TSBICIP-CXRC-024 and TSBICIP-KJGG-007 to L.Z.), CAS Project for Young Scientists in Basic Research (YSBR-072-3 to L.Z.), and Strategic Priority Research Program of the Chinese Academy of Sciences (XDC0120103 to L.Z.).

Author contributions

Experiment, data analysis and writing the initial manuscript were performed by W.L. and K.Z. analyzed data. J.L. provided experimental material. The anaerobic operation was supervised by J.S. Bioelectrocatalytic operation was supervised by Y.W., M.Z., and H.C. Project conception, fund supporting, supervision, and writing the paper were performed by L.Z.

Competing interests

The authors declare no competing interests.

Additional information

Supplementary information The online version contains supplementary material available at <https://doi.org/10.1038/s41467-024-53946-3>.

Correspondence and requests for materials should be addressed to Lingling Zhang.

Peer review information *Nature Communications* thanks Samuel Cobb and the other anonymous reviewer(s) for their contribution to the peer review of this work. A peer review file is available.

Reprints and permissions information is available at <http://www.nature.com/reprints>

Publisher's note Springer Nature remains neutral with regard to jurisdictional claims in published maps and institutional affiliations.

Open Access This article is licensed under a Creative Commons Attribution-NonCommercial-NoDerivatives 4.0 International License, which permits any non-commercial use, sharing, distribution and reproduction in any medium or format, as long as you give appropriate credit to the original author(s) and the source, provide a link to the Creative Commons licence, and indicate if you modified the licensed material. You do not have permission under this licence to share adapted material derived from this article or parts of it. The images or other third party material in this article are included in the article's Creative Commons licence, unless indicated otherwise in a credit line to the material. If material is not included in the article's Creative Commons licence and your intended use is not permitted by statutory regulation or exceeds the permitted use, you will need to obtain permission directly from the copyright holder. To view a copy of this licence, visit <http://creativecommons.org/licenses/by-nc-nd/4.0/>.

© The Author(s) 2024